Niraj Kumar Singh ■ ⑩ ; Victor Hjort ⑩ ; Sanath Kumar Honnali ⑩ ; Davide Gambino ⑩ ; Arnaud le Febvrier ⑩ ; Ganpati Ramanath ⑩ ; Björn Alling ⑩ ; Per Eklund ⑩



J. Appl. Phys. 136, 155301 (2024) https://doi.org/10.1063/5.0226046





# Articles You May Be Interested In

Pt enhanced capacitive performance of Cr<sub>2</sub>N electrode toward flexible asymmetric supercapacitor

Appl. Phys. Lett. (May 2021)

Tailoring structure, morphology, and tribo-mechanical properties of HiPIMS-deposited  $Cr_xN_y$  coatings for enhanced performance in wear and corrosion protection

J. Vac. Sci. Technol. A (May 2024)

Atomic and electronic structures of a transition layer at the CrN/Cr interface

J. Appl. Phys. (August 2011)

02 September 2025 15:47:49





# Effects of W alloying on the electronic structure, phase stability, and thermoelectric power factor in epitaxial CrN thin films

Cite as: J. Appl. Phys. 136, 155301 (2024); doi: 10.1063/5.0226046 Submitted: 28 June 2024 · Accepted: 29 September 2024 · Published Online: 15 October 2024







Niraj Kumar Singh,<sup>1,2,a)</sup> 📵 Victor Hjort,<sup>1</sup> 📵 Sanath Kumar Honnali,<sup>1</sup> 📵 Davide Gambino,<sup>3</sup> 📵 Arnaud le Febvrier,<sup>1</sup> 📵 Ganpati Ramanath, 1,4 🕩 Björn Alling, 3 🕩 and Per Eklund 1,2 🕩





## **AFFILIATIONS**

<sup>1</sup>Thin Film Physics Division, Department of Physics, Chemistry, and Biology (IFM), Linköping University, SE-581 83 Linköping, Sweden

#### **ABSTRACT**

CrN-based alloy thin films are of interest as thermoelectric materials for energy harvesting. *Ab initio* calculations show that dilute alloying of CrN with 3 at. % W substituting Cr induce flat electronic bands and push the Fermi level E<sub>F</sub> into the conduction band while retaining dispersive Cr 3d bands. These features are conducive for both high electrical conductivity  $\sigma$  and high Seebeck coefficient  $\alpha$  and, hence, a high thermoelectric power factor  $\alpha^2 \sigma$ . To investigate this possibility, epitaxial CrW<sub>x</sub>N<sub>z</sub> films were grown on c-sapphire by dc-magnetron  $\frac{1}{2}$ sputtering. However, even films with the lowest W content (x = 0.03) in our study contained metallic h-Cr<sub>2</sub>N, which is not conducive for a  $\frac{10}{25}$ high  $\alpha$ . Nevertheless, the films exhibit a sizeable power factor of  $\alpha^2 \sigma \sim 4.7 \times 10^{-4} \, \mathrm{W m^{-1} K^{-2}}$  due to high  $\sigma \sim 700 \, \mathrm{S \, cm^{-1}}$ , and a moderate  $\alpha \sim -25 \,\mu\text{V/K}$ . Increasing h-Cr<sub>2</sub>N fractions in the  $0.03 < x \le 0.19$  range monotonically increases  $\sigma$ , but severely diminishes  $\alpha$  leading to two orders of magnitude decrease in  $\alpha^2 \sigma$ . This trend continues with x > 0.19 due to W precipitation. These findings indicate that dilute W additions below its solubility limit in CrN are important for realizing a high thermoelectric power factor in CrW<sub>x</sub>N<sub>z</sub> films.

© 2024 Author(s). All article content, except where otherwise noted, is licensed under a Creative Commons Attribution (CC BY) license (https://creativecommons.org/licenses/by/4.0/). https://doi.org/10.1063/5.0226046

## I. INTRODUCTION

Transition metal nitrides (TMNs) constitute an important class of materials that exhibit a combination of high hardness, mechanical strength, thermal stability, and corrosion resistance. TMNs, such as TiN, HfN, and ZrN, have been used as protective and decorative coatings, and nanolayers of metallic TMNs are used as diffusion barriers in nanodevice wiring architectures in integrated circuits.2-5 Narrow-bandgap thin films of TMNs, such as CrN- and ScN-based alloys, have been considered for thermoelectric and piezoelectric energy conversion. 6-9 ScAlN films exhibit large piezoelectric responses at 500 °C, making them suitable for high-temperature device applications. 10-12

Thermoelectric conversion efficiency is related to a dimensionless figure of merit  $ZT = \frac{\alpha^2 \sigma T}{\kappa}$ , where T is the absolute temperature,  $\alpha$  is the Seebeck coefficient,  $\sigma$  is the electrical conductivity,  $\kappa$  is the thermal conductivity,  $^{13,14}$  and  $\alpha^2 \sigma$  is the thermoelectric power factor. Realizing high ZT is a fundamental challenge that requires the circumvention of unfavorable couplings between  $\alpha$ ,  $\sigma$ , and  $\kappa$ . ZT enhancement strategies include doping (less than a few at. %)<sup>15</sup> and/ or alloying (several at. % or more)  $^{16}$  to increase  $\alpha^2 \sigma$  by manipulating the electronic structure, and decreasing  $\kappa$  by impurity- and nanostructuring-induced phonon scattering.

CrN-based alloys have inherently high thermoelectric power factors  $^{19-21}$  due to the narrow bandgap of CrN (E  $_{\!g} \sim 0.2$  eV), which simultaneously induces high  $\sigma$  and high  $\alpha$  underpinned by high charge carrier entropy near the Fermi level  $E_F$ . These attributes, together with an intrinsically low  $\kappa \sim 2~W~m^{-1}~K^{-1}$  when compared to other TMNs,<sup>22</sup> due to low phonon lifetimes arising from spinlattice coupling, <sup>23,24</sup> make CrN an attractive candidate for enhancing

<sup>&</sup>lt;sup>2</sup>Inorganic Chemistry, Department of Chemistry—Ångström Laboratory, Uppsala University, Box 538, SE-751 21 Uppsala, Sweden <sup>3</sup>Theoretical Physics Division, Department of Physics, Chemistry, and Biology (IFM), Linköping University, Linköping 58183, Sweden

<sup>&</sup>lt;sup>4</sup>Rensselaer Polytechnic Institute, Department of Materials Science and Engineering, Troy, New York 12180, USA

<sup>&</sup>lt;sup>a)</sup>Author to whom correspondence should be addressed: niraj-kumar.singh@kemi.uu.se

ZT through doping and alloying. Substituting Cr  $(3d^5)$  with W  $(5d^4)$  in CrN offers the possibility to not only manipulate  $\sigma$  and  $\alpha$  but also decrease  $\kappa$  due to the atomic mass contrast between W and Cr. Indeed, adding W or V to CrN increase  $\alpha^2 \sigma$ , but ZT increases only for W additions which decrease  $\kappa$ , <sup>25</sup> unlike V additions which increase  $\kappa$ . <sup>26</sup> Understanding the effects of W alloying on the electronic structure, phase stability and film morphology are crucial for understanding and tuning the thermoelectric properties to realize high ZT in CrN-based films.

Here, we show from *ab initio* calculations that dilute substitutions of Cr with W in CrN result in flat electronic bands near the Fermi level  $E_F$ , which is pushed into the conduction band. These features are conducive for high  $\sigma$  as well as high  $\alpha$  and, hence, a high power factor  $\alpha^2\sigma$ . To examine this experimentally, we attempted to grow epitaxial  $CrW_xN_z$  films and measured  $\sigma$  and  $\alpha$  as a function of W content x. We find that W additions monotonically increase  $\sigma$  but severely diminish  $\alpha$  due to increasing fractions of metallic  $h\text{-}Cr_2N$  and W precipitation. These findings indicate that restricting W content to below its solubility limit in CrN is crucial for realizing high  $\alpha^2\sigma$  in  $CrW_xN_z$  alloys.

#### II. METHODS

## A. Computational details

The electronic structures of cubic  $Cr_{1-x}W_xN$  with x=0and x = 0.03 in double layer antiferromagnetic (AFM [110]<sub>2</sub>) configuration were computed by density functional theory (DFT) calculations using projector-augmented-wave (PAW) potentials as implemented in the Vienna ab initio simulation package (VASP) code. 27,28 The exchange-correlation energy was treated within the local density approximation with Hubbard term U, (LDA + U) scheme with  $U=3 \text{ eV}^{29}$  to consider Coulombic interactions in the narrow Cr 3d bands and counteract bandgap underestimation or absence by local approaches. The cutoff energy of plane waves for the expansion of wavefunctions was set to 520 eV. Brillouin zone sampling was carried out on a  $5 \times 5 \times 5$  Monkhorst-Pack k mesh, and the electronic optimization criterion was set to  $10^{-5}$  eV. A  $2 \times 2 \times 2$  supercell of 64 atoms was used to analyze the equation of state (EOS) to estimate the equilibrium lattice constant  $a_0$ . The crystal structure was visualized using Vesta<sup>30</sup> and the electronic structures were plotted using Sumo package.3

# B. Experimental details

CrW<sub>x</sub>N<sub>z</sub> thin films with 0 ≤ x ≤ 0.25 were grown in an ultrahigh vacuum chamber with a base pressure of ~10<sup>-6</sup> Pa by DC-magnetron sputtering onto 10 × 10 mm² c-plane sapphire substrates (Alineason Materials Technologies). Prior to film growth, the substrates were ultrasonicated successively in acetone and ethanol for 10 min each, followed by blow drying with a N₂ gas jet. The films were sputter-deposited from 50-mm-diameter disk-shaped targets of Cr and W (both 99.95% purity) using a 0.33 Pa (~2.5 mTorr) plasma struck with a 40/60 Ar/N₂ mixture. The W level was varied by fixing the Cr target power P<sub>Cr</sub> constant and varying the W target power P<sub>W</sub> in the 0.1 ≤ P<sub>W</sub>/P<sub>Cr</sub> ≤ 0.65 range. During film deposition, the substrates were at 600 °C and rotated at 15 rpm.

Phase purity and crystal structure were characterized by x-ray diffractometry (XRD) using a PANanlytical X'Pert Pro instrument with a Cu- $K_{\alpha}$  radiation source operated at 45 kV and 40 mA. Pole figure measurements were carried out by scanning along in-plane rotation  $\varphi$  and out-of-plane tilt  $\psi$  angles at 2.5° steps per second using cross-slit primary optics and parallel plate collimator secondary optics. Film thickness, roughness, and density were estimated by analyses of x-ray reflectivity (XRR) data acquired using a hybrid-mirror module with a 0.5° incidence slit and a 0.125° post-diffraction slit.

Film morphology was examined by scanning electron microscopy (SEM) in a Sigma 300 Zeiss instrument operated at 3 kV using Inlens detector. We carried out energy dispersive x-ray spectroscopy (EDX) in the SEM for qualitative compositional mapping. We note that EDX in the SEM is unsuited for quantitative analysis of thin films on a thick substrate because substrate-induced absorption and fluorescence predominate and confound the signal from film.<sup>32</sup>

Film composition was determined from a combination of Rutherford backscattering spectrometry (RBS) and time-of-flight elastic recoil detection analysis (ToF-ERDA), which allow quantification without the use of standards. RBS experiments were carried out using a 15-SDH2 Pelletron accelerator at Tandem Laboratory, Uppsala University. A 2 MeV He<sup>+</sup> primary ion beam was incident at 5° to the sample normal, and the backscattered particles were detected at 170°. The spectra were analyzing using fits from SIMNRA simulations. For ToF-ERDA measurements, a 44 MeV 136 I<sup>8+</sup> beam was incident at an angle of 67.5° with the sample surface normal. The recoiled ions were detected with a ToF system placed at 45° with respect to the incident beam. Elemental depth profiles were extracted from the time and energy coincidence ERDA spectra using Potku 2.0 code.

Room-temperature electrical conductivity  $\sigma$  was measured by using a Jandel Model RM3000 four-point-probe station. Seebeck coefficient,  $\sigma$ , was measured using a home-made setup equipped with Peltier devices that maintain desired temperature gradient across the sample. In this setup, temperatures are measured with K-type thermocouples, and the Seebeck voltage is measured with a Keithley 2001 multimeter as described elsewhere. The Charge carrier density  $\sigma$  and mobility  $\sigma$  were measured by room-temperature Hall measurements in a home-made setup with a 0.485 T permanent magnet. The Hall voltage was measured in the van der Pauw configuration with a Keithley 2100 multimeter for a 40 mA current supplied by a Keithley 2400 source.

# III. RESULTS AND DISCUSSION

## A. Ab initio calculations

CrN undergoes a magnetostructural transition at the Néel temperature  $T_{\rm N}\sim 280$  K, wherein the antiferromagnetic low-temperature orthorhombic phase is converted to the high-temperature paramagnetic rock salt phase. However, cubic CrN is known to energetically favor the antiferromagnetic spin configuration with alternating double layers of identical spin perpendicular to the crystallographic [110] direction (AFM-110<sub>2</sub>) as shown in Fig. 1(a). The equilibrium lattice parameter  $a_0$  of cubic CrN was estimated by fitting energy (E) vs volume (V) to obtain  $a_0 \sim 4.13$  Å for CrN [Fig. 1(b)], which agrees well with prior theoretical and experimental reports.  $^{39,40}$  For

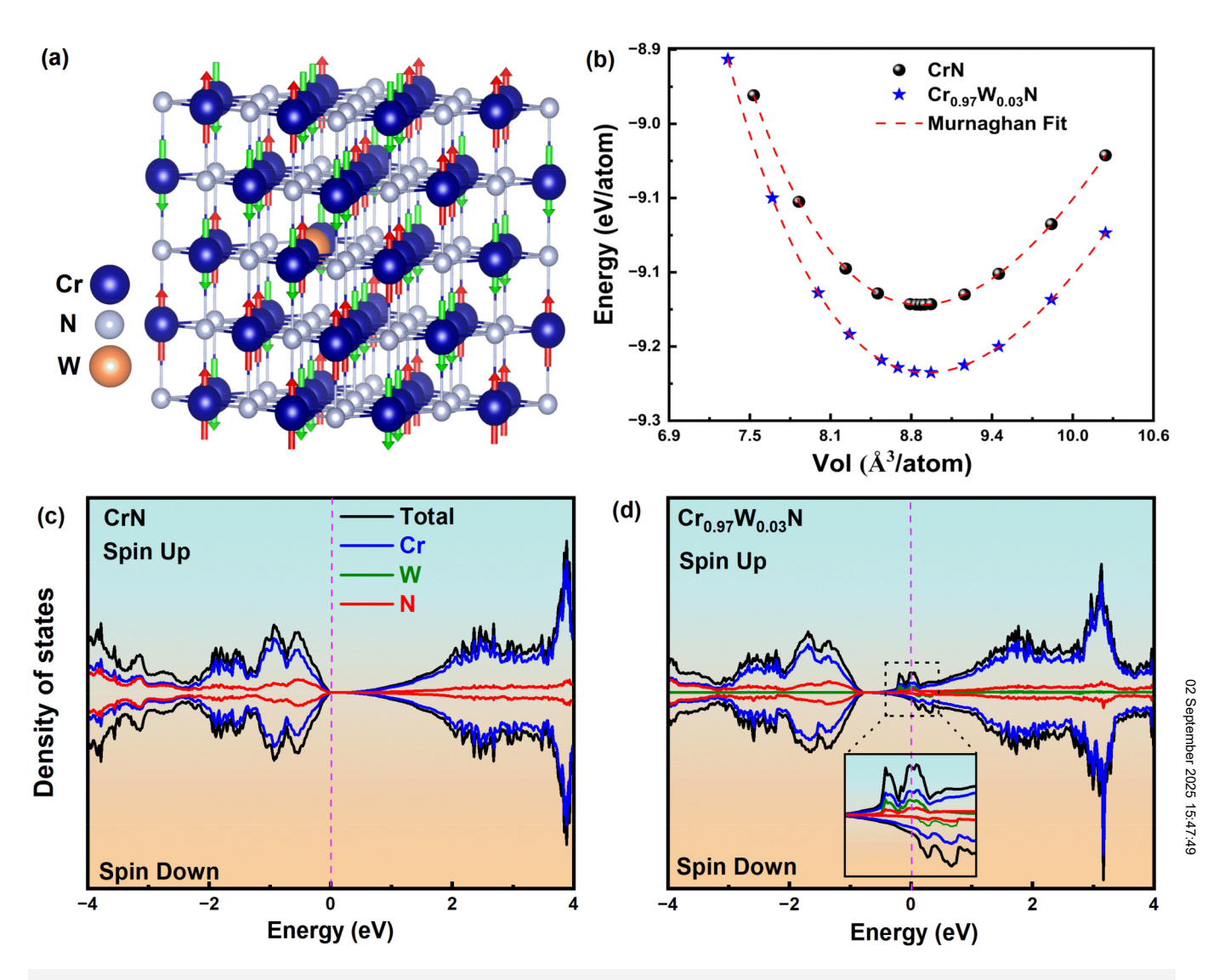


FIG. 1. (a) A sketch of the cubic CrN crystal structure showing Cr↑ (red) and Cr↓ (green) sites, with W substitution at the Cr↑ sites. (b) Murnaghan fits for CrN and Cr<sub>0.97</sub>W<sub>0.03</sub>N. Density of states plots for (c) CrN and (d) Cr<sub>0.97</sub>W<sub>0.03</sub>N with inset showing a zoomed-in view near E<sub>F</sub>

 $Cr_{1-x}W_xN$  with x = 0.03, we obtain  $a_0 \sim 4.14$  Å for W occupancy of either Cr\u2224 or Cr\u2224 sites, suggesting no observable site-occupancy effect. Thus, we calculated the electronic properties only for W substitution at Cr↑ sites.

For pristine defect-free CrN, the calculated bandgap  $E_g \sim 0.2 \text{ eV}$  agrees with prior work, <sup>41</sup> and the Cr 3d states are the primary contributors to the states near E<sub>F</sub> [see Fig. 1(c)]. Substituting Cr with 3 at. % W, i.e., x = 0.03, pushes the  $E_F$  inside the conduction band [Fig. 1(d)] and results in a higher density of states (DOS) in a narrow energy band near E<sub>F</sub> [see inset of Fig. 1(d)] than in CrN. The W-induced E<sub>F</sub> shift into the conduction band is likely to produce metal-like electrical transport, commonly observed in degenerate semiconductors.

Electronic structure calculations for CrN along the high symmetry X-Γ-K-W-X path reveal dispersive Cr 3d bands with conduction band minima at  $\Gamma$ , and a bandgap of  $E_g \sim 0.2 \, eV$  [Fig. 2(a)]. Alloying with 3 at. % W largely preserves the CrN band structure, but creates additional flatbands with a strong W-d character near E<sub>F</sub> [Fig. 2(b)], consistent with the aforementioned W-alloying-induced DOS increase near E<sub>F</sub>. We note that the W-induced flatbands arise from the hybridization of W 3d, Cr 3d, and N 2p orbitals, whereas Cr 3p and 3d states also contribute to dispersive bands at  $\Gamma$ [Fig. 2(c)]. These results suggest that the W content should be dilute enough to maintain a judicious balance of both dispersive and flatbands to realize high  $\alpha^2 \sigma$ . W-induced flatbands would entail high charge carrier effective masses m\* conducive for high

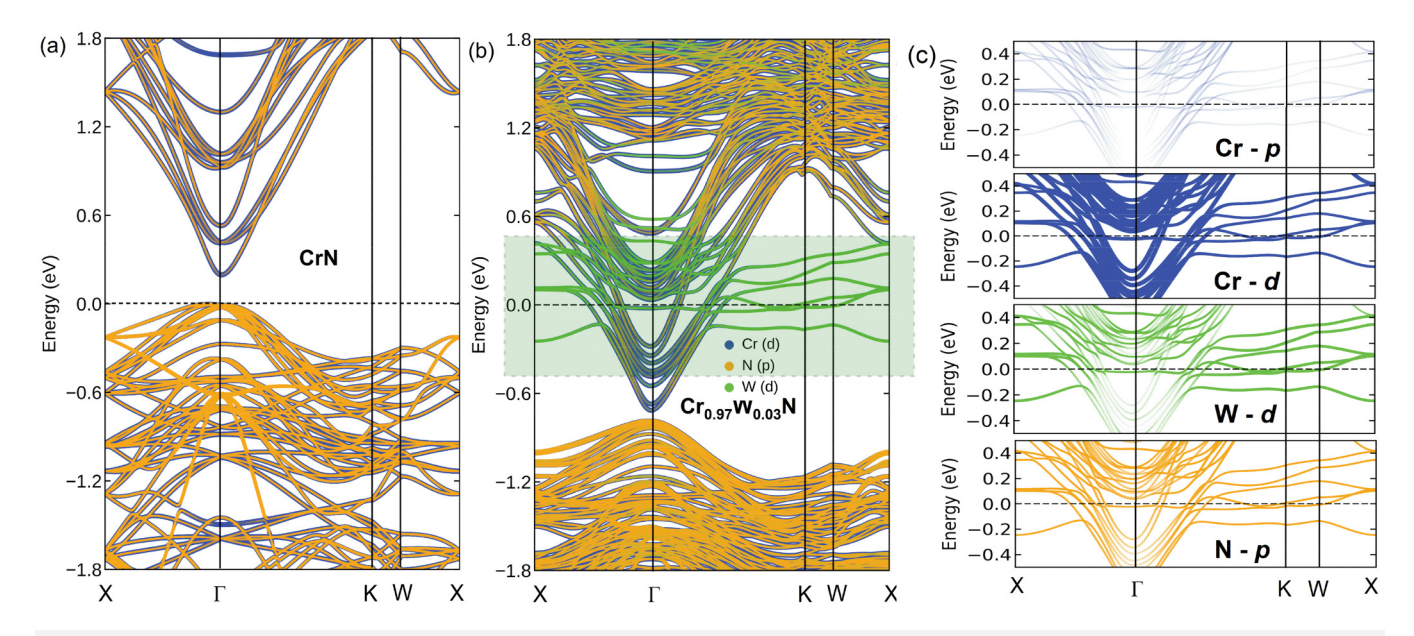


FIG. 2. Electronic band structures computed by ab initio calculations along X-Γ-K-W-X for (a) CrN and (b)  $Cr_{0.97}W_{0.03}N$ . (c) Individual contributions from Cr, W, and N orbitals to the electronic bands in the  $E_F \pm 0.5$  eV range for  $Cr_{0.97}W_{0.03}N$ .

 $\alpha,$  as seen from  $\alpha = \frac{8\pi^2 k_B^2}{3eh^2} m^* T \left(\frac{\pi}{3n}\right)^{\frac{2}{3}},$  where n is the charge carrier density. However, retention of adequate dispersive bands from Cr is needed for high charge carrier mobility  $\mu$  and high electrical conductivity  $\sigma.^{43}$ 

## B. Epitaxial CrW<sub>x</sub>N growth and structural analysis

To experimentally investigate our theoretical predictions, we attempted to grow epitaxial  $Cr_{1-x}W_xN_\delta$  films. We chose a growth temperature of 600 °C because epitaxial rock salt CrN is favored in the 550 °C  $\leq$  T  $\leq$  700 °C range,  $^{44}$  and metallic  $\emph{h}\text{-}Cr_2N$  formation at higher temperatures is not conducive for high  $\alpha$ . Cr target power  $P_{Cr}$  is also a crucial parameter that influences CrN and  $\emph{h}\text{-}Cr_2N$  phase selection and fractions, and Cr vacancy concentration that can impact electronic conductivity  $\sigma$ . Results of our studies of CrN films grown with 42 W  $\leq$   $P_{Cr}$   $\leq$  50 W showed that the highest  $\alpha^2\sigma$  was obtained for  $P_{Cr}$  = 44 (see Fig. S1 in the supplementary material). Accordingly,  $CrW_xN_z$  films were deposited for different  $P_W$  at a fixed  $P_{Cr}$  = 44 W.

RBS and ERDA analyses showed that all the  $CrW_xN_z$  films were nitrogen-deficient [see Fig. 3(a)]. Increasing  $P_W$  in the  $0.1 \le P_W/P_{Cr} \le 0.65$  range increased the W content from x=0.03 to 0.25, decreased the nitrogen content from z=0.91 to 0.21, and increased oxygen contamination from 1.7 to 5.5 at. %. The large decreases in nitrogen content correlating with increasing W content suggests the formation of a Cr-rich  $Cr_2N$ , corroborated by XRD analyses described below.

X-ray diffractograms show that W additions shift the 111 and 222 CrN Bragg peaks to higher angles, i.e., lower d-spacings, indicative of W-induced unit cell compression. Even for  $x \sim 0.03$ , the

lowest W content explored in this study, we observe the  $h\text{-}\mathrm{Cr}_2\mathrm{N}$   $^{80}_{90}$  (0002) reflection at  $2\theta \sim 40.3^\circ$ . The results indicate that the solubility limit of W in CrN is less than  $x \sim 0.03$  even under the far-from equilibrium conditions involved during sputter deposition. Low solubility of W in CrN according is consistent with the large differences in cationic sizes and electronegativity for Cr and W. Our attempts to obtain CrN films with lower W contents were unsuccessful due to the instability of the plasma at low  $P_{\mathrm{W}}$ . Alternative approaches such as pulsed sputtering, ion-implantation, and hybrid techniques that independently introduce the dilute alloying element, e.g., WF<sub>6</sub> gas into the plasma,  $^{46}$  are possible strategies to achieve dilute W concentrations in CrN films.

At x = 0.07, the CrN peaks continue to shift further but considerably decrease in intensity, while the  $h\text{-Cr}_2N$  0002 peak intensity increases and the  $h\text{-Cr}_2N$  0004 peak appears at  $2\theta \sim 86.5^\circ$ . No rock salt CrN peaks were detectable in diffractograms from films with x = 0.19, whereas the  $h\text{-Cr}_2N$  peaks were stronger. Films with x = 0.25 exhibit 110 and 220 Bragg peaks at  $2\theta \sim 40.55^\circ$  and  $\sim 88.1^\circ$  from metallic W, showing the coexistence of metallic  $h\text{-Cr}_2N$  and W.

X-ray pole figure scans around 111 and  $03\bar{3}1$  reflections from the CrN<sub>z</sub> and CrW<sub>0.25</sub>N<sub>z</sub> films, respectively, show distinct spot patterns at specific angles (Fig. 4). These results show a high degree of preferred orientation of the grains confirming the epitaxial growth of CrN<sub>z</sub> and CrW<sub>x</sub>N<sub>z</sub> films. Scans from epitaxial CrN films around the (111) pole show a central peak surrounded by six {111} peaks at a radial angle of  $\psi \sim 71^\circ$  [Fig. 4(a)] with each of the adjacent spots separated azimuthally by  $\Delta \varphi = 60^\circ$ . This spot pattern indicates epitaxial rock salt structured crystals with two twin orientations of on *c*-sapphire, as reported elsewhere.<sup>47</sup> Spots connected by dotted lines in Fig. 4(a) connote one of the two twin domains. Pole

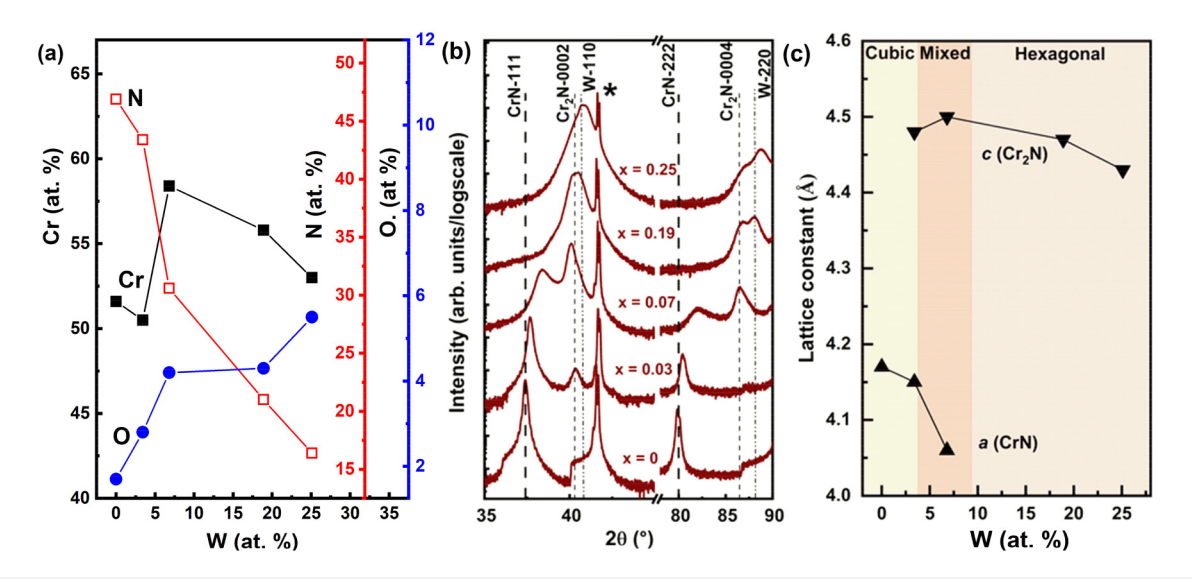


FIG. 3. (a) Elemental concentrations of Cr (black), N (red), and O (blue) determined by RBS and ERDA and plotted as a function of W concentration. (b) X-ray diffractograms from  $CrW_xN_z$  films with  $0.00 \le x \le 0.25$ , where \* connotes the c-sapphire 006 peak at  $2q \sim 41.67^\circ$ . (c) Lattice parameters of CrN and h-Cr<sub>2</sub>N for  $CrW_xN_z$  films for W concentrations in the  $0.00 \le x \le 0.25$  range.

figures from  $CrW_{0.25}N_z$  films reveal six poles at  $\psi \sim 65^{\circ}$  consisting of three sets of doublets separated azimuthally by  $\Delta \phi = 120^{\circ}$ , implying threefold symmetry, wherein the inter-doublet separation is  $\Delta \phi \sim 36^{\circ}$  [Fig. 4(b)]. These characteristics indicate that even the h-Cr<sub>2</sub>N phase bears an epitaxial relationship with the substrate. These observations suggest that W alloying stimulates Cr<sub>2</sub>N crystal formation from epitaxial CrN, consistent with prior reports of epitaxial inclusions and in-plane heterostructures of h-Cr2N in epitaxial CrN thin films. 48,4

Analyses of XRR data (see Fig. S1 in the supplementary S material) show that all the  $CrW_xN_z$  films were  $\sim 60$  nm thick  $\frac{60}{50}$  with a roughness of  $\leq 3$  nm, irrespective of the W content.  $\frac{60}{50}$  The film density increased from  $\sim 6.7$  to 11.1 g cm<sup>-3</sup> as the W  $\frac{60}{50}$ content was increased from x = 0.03 to x = 0.25. The baseline

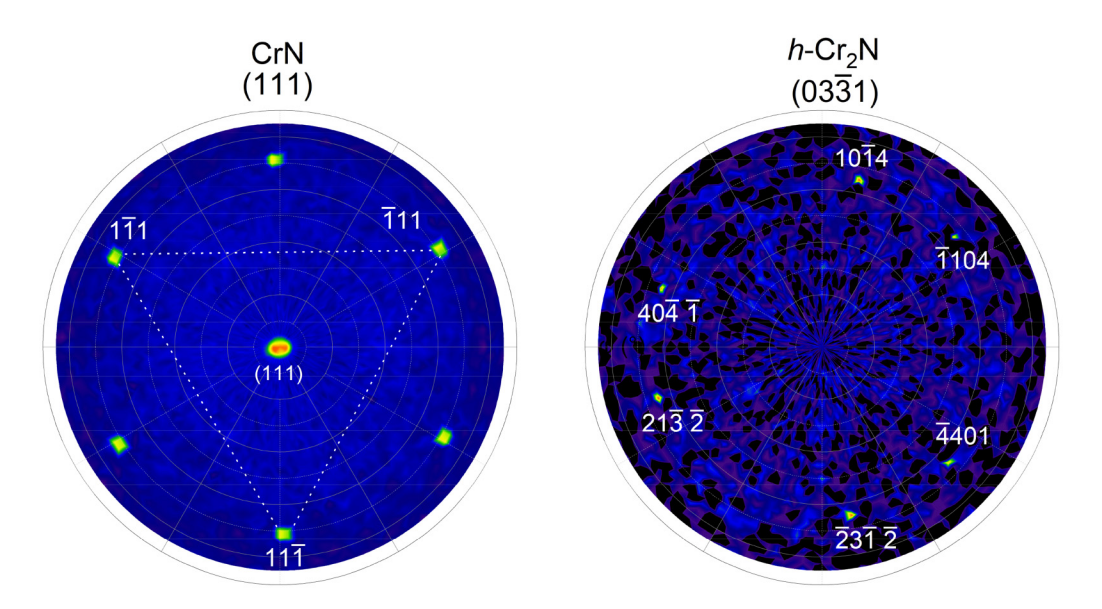


FIG. 4. Representative pole figure scans from (a) epitaxial CrN<sub>z</sub> on c-sapphire around the CrN (111) Bragg reflection with 20 = 37.4° and (b) epitaxial CrW<sub>0.25</sub>N<sub>z</sub> on c-sapphire around the h-Cr<sub>2</sub>N (0331) reflection with 20 = 73.1°. In (a), the two sets of triplets (dotted lines indicate one triplet) correspond to two twin variants of epitaxial CrN.

density for CrN films was  $\sim 5.8 \,\mathrm{g \, cm^{-3}}$ , which is  $\sim 98\%$  of the theoretical density of CrN.

## C. Morphological studies

W alloying had a significant effect on the epitaxial CrW<sub>x</sub>N<sub>z</sub> film morphology. Pristine epitaxial CrN film surfaces exhibit large triangular grains [Fig. 5(a)] indicative of 111-oriented rock salt films. 50 In contrast, films with x = 0.03 show highly elongated grains with an average width of ~70 nm; however, the average lengths of these grains are difficult to calculate due to continuous and curved domains [Fig. 5(b)]. These observations viewed in light of our pole figure results indicate that our epitaxial films are comprised of nanocrystalline grains with high degrees of preferred orientations. EDX maps of W and Cr from  $CrW_xN_z$  films with x = 0.03 (Fig. S3 in the supplementary material) show homogenous contrast attributable to dissolved W, consistent with our XRD results indicating no observable W precipitation at x = 0.03.

Films with higher W contents show a different morphology indicative of fine h-Cr<sub>2</sub>N grains. However, for x = 0.07, we observe a dense morphology [Fig. 5(c)]. Films with x = 0.19 and 0.25[Figs. 5(d) and 5(e)] both exhibit similar features having average grain size ~40 nm, but with the presence of voids. Increasing the W content leads to grain refinement, h-Cr2N formation and W precipitation. The grain size distribution for the corresponding films is plotted in Figs. 5(f)-5(h). No selective grain boundary precipitation of W is discernible from EDX maps showing homogenous W and Cr distributions (see Fig. S4 in the supplementary material) with no observable correlation with grain boundary contrast [Fig. 5(e)].

#### D. Thermoelectric transport properties

The room-temperature values of  $\sigma$  and  $\alpha$  measured from the films are plotted in Fig. 6 as a function W alloying content. Pristine CrN shows  $\sigma \sim 197 \, \mathrm{S \, cm^{-1}}$ , which agrees with prior reports for CrN films deposited under similar conditions.<sup>21</sup> Adding W increases σ to  $\sim 700 \,\mathrm{S\,cm}^{-1}$  for x = 0.03, which is in accordance with the W-induced changes in the electronic band structure and increase in the density of states at the Fermi level indicated by our ab initio calculations. For x > 0.03, however, our theoretical calculations do not directly apply because of h-Cr2N phase formation that was not considered in our computations. Films with higher W contents in the  $0.07 \le x \le 0.19$  range exhibit no considerable changes in  $\sigma$  suggesting that the increase in σ expected from increased metallic h-Cr<sub>2</sub>N fraction is countered by the decreased rock salt CrN fraction. At x = 0.25,  $\sigma$  increases to  $\sim 1800 \text{ S cm}^{-1}$  due to W precipitation.

The thermoelectric properties and the Hall measurement analyses are shown in Fig. 5. All the films show negative α, indicating n-type behavior, i.e., electrons are the majority charge carriers. Pristine CrN shows high  $\alpha \sim -155 \,\mu\text{V/K}$ , which reduces greatly to  $\alpha \sim -25 \,\mu\text{V/K}$  for x = 0.03. Experimental observation of lower  $\alpha$ for x = 0.03 as contrary to the theoretical calculations infers that one needs to explore much lower W content CrN films to avoid

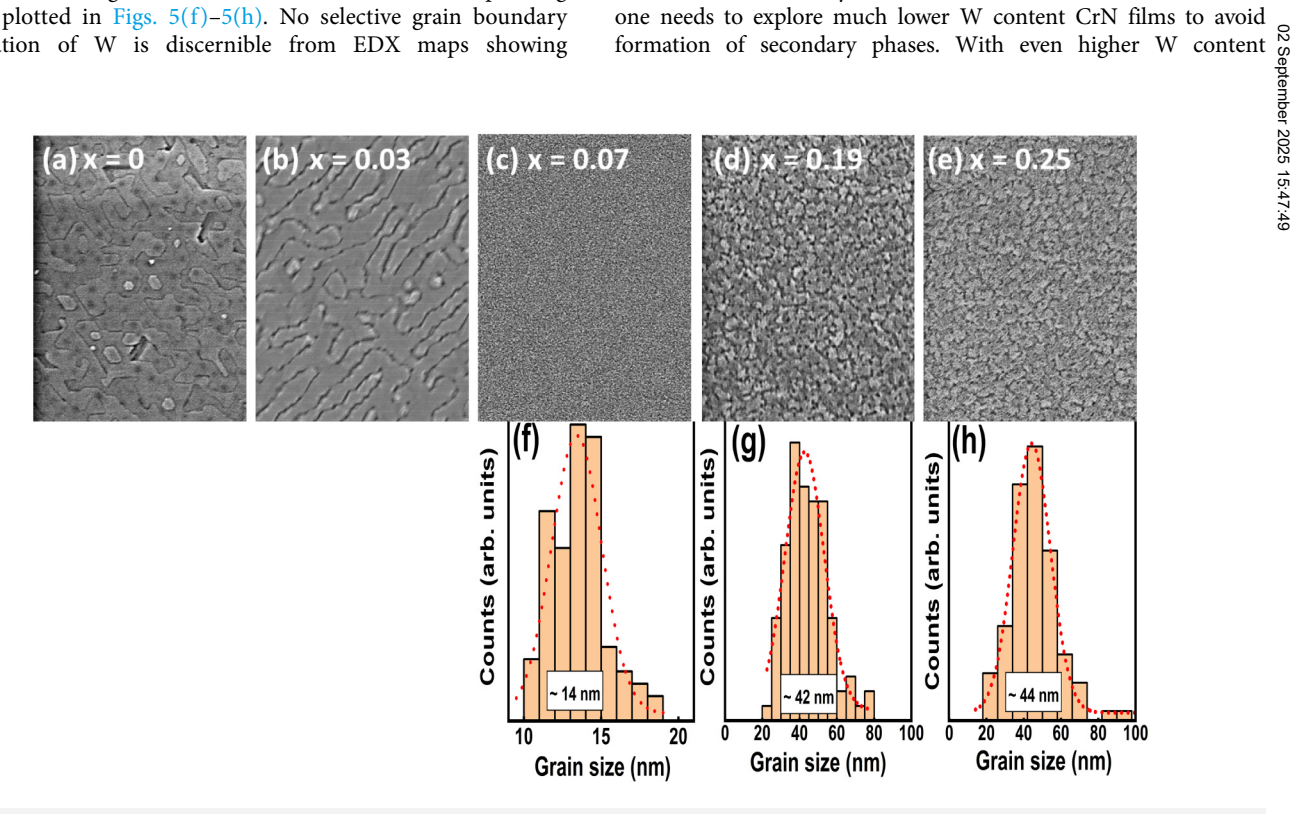


FIG. 5. (a)–(e) SEM micrographs from  $CrW_xN_z$  films with  $0.00 \le x \le 0.25$ , and (f)–(h) corresponding grain size distribution plot with Gaussian fit.

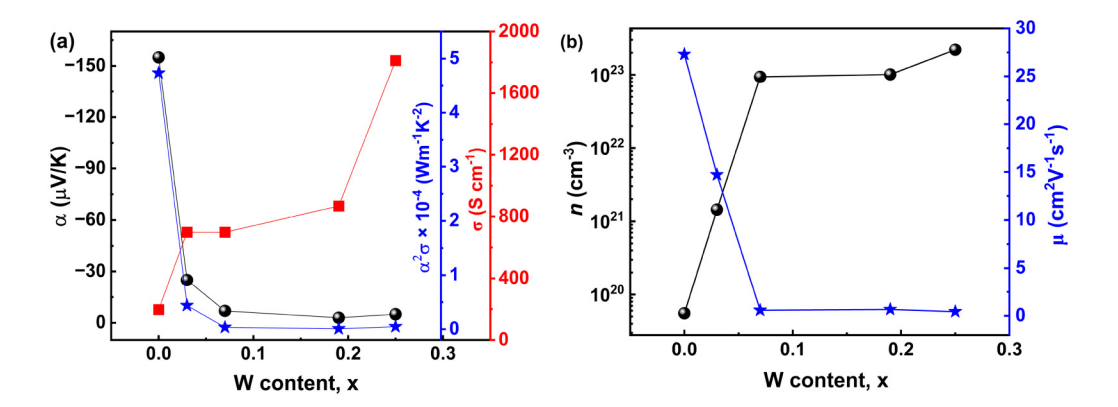


FIG. 6. (a) Seebeck coefficient, electrical conductivity, and corresponding power factor, and (b) carrier density n and mobility  $\mu$  extracted from Hall measurements in CrWxNz films.

(x > 0.03),  $\alpha$  reduces further and saturates around  $\alpha \sim 5 \,\mu\text{V/K}$  due to the increased metallic h-Cr<sub>2</sub>N phase.

The room-temperature power factor  $\alpha^2 \sigma \sim 4.7 \times 10^{-4} \text{ W m}^{-1} \text{ K}^{-2}$ for CrN is in close agreement as reported by Kerdsongpanya et al.  $(\sim 5 \times 10^{-4} \,\mathrm{W m^{-1} \, K^{-2}})^{21}$  but lower than those of Gharavi et al.  $(\sim 9-11 \times 10^{-3} \text{ W m}^{-1} \text{ K}^{-2})$ . However, due to the reduced  $\alpha$ , all films with W show lowered  $\alpha^2 \sigma$  values.

Analyses of Hall measurements of the CrW<sub>x</sub>N<sub>z</sub> films [Fig. 5(b)] indicate W additions result in a up to four-orders-of-magnitude increase in charge carrier density n, accompanied by a two-orders of magnitude decrease in carrier mobility  $\mu$ . The large increase in carrier density is attributed to metallic h-Cr<sub>2</sub>N<sup>48</sup> and W precipitation. The increasing nitrogen deficiency in increasing W content suggests that N vacancies, known to be electron donors in CrN could also be a contributing factor.45

The measured  $n \sim 5.5 \times 10^{19} \text{ cm}^{-3}$  for CrN agrees well with prior reports [21]. The low  $\mu$  is typical of metals and is attributable to grain boundary and W impurity scattering mechanisms. Since α and  $\sigma$  are strongly and adversely coupled through n, the monotonic rise in n increases  $\sigma$  but decreases  $\alpha$ , leading to a net decrease in  $\alpha^2 \sigma$ . Thus, it is crucial to restrict W additions to below its solubility limit in CrN to preclude the formation of h-Cr2N and W precipitation to realize high  $\alpha^2 \sigma$ .

# **IV. CONCLUSIONS**

Ab initio calculations indicate that dilute W additions to CrN are attractive to increase the thermoelectric power factor due to the emergence of flat bands near the Fermi level pushed into the conduction band. Epitaxial growth of dc-magnetron sputtered W alloyed CrN films showed metallic h-Cr2N formation even for the smallest W contents explored in this study. Despite this, the power factor is considerable at x = 0.08 due to high  $\sigma \sim 700 \, \text{S cm}^{-1}$  and sizeable  $\alpha = -25 \,\mu\text{V/K}$ . Increasing W content severely diminishes  $\alpha$ despite the monotonic increase in  $\sigma$  due to increasing h-Cr<sub>2</sub>N fraction and W precipitation. These findings indicate that limiting W alloying to below its solubility limit in CrN is crucial for realizing a high power factor.

#### SUPPLEMENTARY MATERIAL

The supplementary material includes details of CrN film growth as a function of Cr target power P<sub>Cr</sub>, and their thermoelectric power factor. It also presents analyses of x-ray reflectograms from CrWxNz films to determine film thickness, roughness and density, and EDX maps of films with the highest W content.

# **ACKNOWLEDGMENTS**

KNOWLEDGMENTS

The authors acknowledge funding from the Swedish Government Strategic Research Area in Materials Science on Sunctional Materials at Linköping University (Faculty Grant SFO-Mat-LiU No. 2009 00971), the Knut and Alice Wallenberg  $\frac{\vec{o}}{4}$ foundation through the Wallenberg Academy Fellows program 3 (KAW-2020.0196), the Swedish Research Council (VR) under Project No. 2021-03826, and the Swedish Energy Agency under Project No. 52740-1. N.K.S. and P.E. acknowledge support from the Foundation Olle Engkvist Byggmästare (Grant No. 218-0076). N.K.S. acknowledges Dr. Rui Shu for his help during the initial experimental phase. G.R. gratefully acknowledges funding from the U.S. National Science Foundation (Grant No. CMMI 2135725) through the BRITE program. D.G. acknowledges support from the Swedish Research Council (VR) International Postdoc (Grant No. 2023-00208). B.A. acknowledges financial support from the Swedish Research Council (VR) through Grant Nos. 2019-05403 and 2023-05194. The computations were enabled by resources provided by the National Academic Infrastructure for Supercomputing in Sweden (NAISS), at the National Supercomputer Center (NSC), partially funded by the Swedish Research Council through Grant Agreement No. 2022-06725.

# **AUTHOR DECLARATIONS Conflict of Interest**

The authors declare no conflict of interest.

#### **Author Contributions**

Niraj Kumar Singh: Conceptualization (equal); Data curation Formal analysis (equal); Investigation Methodology (equal); Writing - original draft (equal). Victor Hjort: Data curation (equal); Investigation (equal); Methodology (equal); Writing - review & editing (equal). Sanath Kumar Honnali: Data curation (equal); Formal analysis (equal); Writing review & editing (equal). Davide Gambino: Methodology (equal); Supervision (equal); Writing - review & editing (equal). Arnaud le Febvrier: Data curation (equal); Formal analysis (equal); Methodology (equal); Project administration (equal); Supervision (equal); Writing - review & editing (equal). Ganpati Ramanath: Supervision (equal); Writing - review & editing (equal). Björn Alling: Funding acquisition (equal); Resources (equal); Software (equal); Supervision (equal); Writing - review & editing (equal). Per Eklund: Conceptualization (equal); Funding acquisition (equal); Project administration (equal); Resources (equal); Supervision (equal); Validation (equal); Writing - review & editing (equal).

#### DATA AVAILABILITY

The data that support the findings of this study are available from the corresponding author upon reasonable request.

#### **REFERENCES**

- <sup>1</sup>R. S. Ningthoujam and N. S. Gajbhiye, Prog. Mater. Sci. 70, 50–154 (2015).
- <sup>2</sup>D. D. Kumar, N. Kumar, S. Kalaiselvam, S. Dash, and R. Jayavel, Surf. Interfaces 7, 74–82 (2017).
- <sup>3</sup>F. Lévy, P. Hones, P. E. Schmid, R. Sanjinés, M. Diserens, and C. Wiemer, Surf. Coat. Technol. **120–121**, 284–290 (1999).
- <sup>4</sup>M. A. Vasylyev, B. N. Mordyuk, S. I. Sidorenko, S. M. Voloshko, A. P. Burmak, I. O. Kruhlov, and V. I. Zakiev, Surf. Coat. Technol. **361**, 413–424 (2019).
- <sup>5</sup>G. Wang, Y. Si, M. Wen, J. Qiu, S. Zhang, Q. Song, W. Wang, X. Yang, and P. Ren, J. Mater. Res. Technol. 22, 2030–2042 (2023).
- <sup>6</sup>S. Kerdsongpanya, N. Van Nong, N. Pryds, A. Žukauskaitė, J. Jensen, J. Birch, J. Lu, L. Hultman, G. Wingqvist, and P. Eklund, Appl. Phys. Lett. **99**, 232113 (2011).
- <sup>7</sup>P. V. Burmistrova, J. Maassen, T. Favaloro, B. Saha, S. Salamat, Y. Rui Koh, M. S. Lundstrom, A. Shakouri, and T. D. Sands, J. Appl. Phys. **113**, 153704 (2013).
- <sup>8</sup>C. X. Quintela, B. Rodríguez-González, and F. Rivadulla, Appl. Phys. Lett. 104, 022103 (2014).
- <sup>9</sup>C. X. Quintela, J. P. Podkaminer, M. N. Luckyanova, T. R. Paudel, E. L. Thies, D. A. Hillsberry, D. A. Tenne, E. Y. Tsymbal, G. Chen, C.-B. Eom, and F. Rivadulla, Adv. Mater. 27, 3032–3037 (2015).
- <sup>10</sup>M. Akiyama, T. Kamohara, K. Kano, A. Teshigahara, Y. Takeuchi, and N. Kawahara, Adv. Mater. 21, 593–596 (2009).
- <sup>11</sup>F. Tasnádi, B. Alling, C. Höglund, G. Wingqvist, J. Birch, L. Hultman, and I. A. Abrikosov, Phys. Rev. Lett. 104, 137601 (2010).
- <sup>12</sup>A. Zukauskaite, G. Wingqvist, J. Palisaitis, J. Jensen, P. O. Å. Persson, R. Matloub, P. Muralt, Y. Kim, J. Birch, and L. Hultman, J. Appl. Phys. 111, 093527 (2012).
- <sup>13</sup>G. J. Snyder and E. S. Toberer, Nat. Mater. 7, 105–114 (2008).
- <sup>14</sup>S. Bathula, M. Jayasimhadri, B. Gahtori, N. K. Singh, K. Tyagi, A. K. Srivastava, and A. Dhar, Nanoscale 7, 12474–12483 (2015).
- <sup>15</sup>R. J. Mehta, Y. Zhang, C. Karthik, B. Singh, R. W. Siegel, T. Borca-Tasciuc, and G. Ramanath, Nat. Mater. 11, 233–240 (2012).
- <sup>16</sup>D. Wines, F. Ersan, and C. Ataca, ACS Appl. Mater. Interfaces 12, 46416–46428 (2020).

- <sup>17</sup>J. R. Sootsman, D. Y. Chung, and M. G. Kanatzidis, Angew. Chem. Int. Ed. 48, 8616–8639 (2009).
- <sup>18</sup>C. J. Vineis, A. Shakouri, A. Majumdar, and M. G. Kanatzidis, Adv. Mater. 22, 3970–3980 (2010).
- 19P. Eklund, S. Kerdsongpanya, and B. Alling, J. Mater. Chem. C 4, 3905–3914 (2016).
- <sup>20</sup>S. Kerdsongpanya, B. Alling, and P. Eklund, Phys. Rev. B **86**, 195140 (2012).
- <sup>21</sup>S. Kerdsongpanya, B. Sun, F. Eriksson, J. Jensen, J. Lu, Y. K. Koh, N. V. Nong, B. Balke, B. Alling, and P. Eklund, J. Appl. Phys. 120, 215103 (2016).
- <sup>22</sup>W. Lengauer, Encyclopedia of Inorganic and Bioinorganic Chemistry (Wiley, 2015), p. 1.
- <sup>23</sup>I. Stockem, A. Bergman, A. Glensk, T. Hickel, F. Körmann, B. Grabowski, J. Neugebauer, and B. Alling, Phys. Rev. Lett. 121, 125902 (2018).
- <sup>24</sup>O. Jankovský, D. Sedmidubský, Š Huber, P. Šimek, and Z. Sofer, J. Eur. Ceram. Soc. 34, 4131–4136 (2014).
- <sup>25</sup>C. X. Quintela, F. Rivadulla, and J. Rivas, Appl. Phys. Lett. **94**, 152103 (2009).
- <sup>26</sup>F. Rivadulla, M. Bañobre-López, C. X. Quintela, A. Piñeiro, V. Pardo, D. Baldomir, M. A. López-Quintela, J. Rivas, C. A. Ramos, H. Salva, J.-S. Zhou, and J. B. Goodenough, Nat. Mater. 8, 947–951 (2009).
- <sup>27</sup>G. Kresse and J. Hafner, Phys. Rev. B 47, 558–561 (1993).
- 28G. Kresse and J. Furthmüller, Comput. Mater. Sci. 6, 15–50 (1996).
- <sup>29</sup>S. L. Dudarev, G. A. Botton, S. Y. Savrasov, C. J. Humphreys, and A. P. Sutton, Phys. Rev. B **57**, 1505–1509 (1998).
- **30**K. Momma and F. Izumi, J. Appl. Crystallogr. **44**, 1272–1276 (2011).
- <sup>31</sup>Alex M. Ganose, Adam J. Jackson, and David O. Scanlon, J. Open Source Software 3, 717 (2018).
- 32 E. Lifshin and R. Gauvin, Microsc. Today 11, 46–49 (2003).
- <sup>33</sup>L. C. F. Terry, L. Alford, and J. W. Mayer, Fundamentals of Nanoscale Film Analysis (Springer, 2007).
- 34P. Ström and D. Primetzhofer, J. Instrum. 17, P04011 (2022).
- 35 M. Mayer, AIP Conf. Proc. 475, 541–544 (1999).
- <sup>36</sup>K. Arstila, J. Julin, M. I. Laitinen, J. Aalto, T. Konu, S. Kärkkäinen, S. Rahkonen, M. Raunio, J. Itkonen, J. P. Santanen, T. Tuovinen, and T. Sajavaara, Nucl. Instrum. Methods Phys. Res. Sect. B 331, 34–41 (2014).
- <sup>37</sup>B. Xin, A. Le Febvrier, L. Wang, N. Solin, B. Paul, and P. Eklund, Mater. Des. 210, 110033 (2021).
- 38 A. S. Botana, F. Tran, V. Pardo, D. Baldomir, and P. Blaha, Phys. Rev. B 85, 235118 (2012).
- <sup>39</sup>B. Alling, T. Marten, and I. A. Abrikosov, Phys. Rev. B 82, 184430 (2010).
- 40 L. M. Corliss, N. Elliott, and J. M. Hastings, Phys. Rev. 117, 929–935 (1960).
- <sup>41</sup>L. Zhou, F. Körmann, D. Holec, M. Bartosik, B. Grabowski, J. Neugebauer, and P. H. Mayrhofer, Phys. Rev. B 90, 184102 (2014).
- <sup>42</sup>G. D. Mahan and J. O. Sofo, Proc. Natl. Acad. Sci. U.S.A. 93, 7436–7439 (1996).
- <sup>43</sup>A. Gaul, Q. Peng, D. J. Singh, G. Ramanath, and T. Borca-Tasciuc, Phys. Chem. Chem. Phys. **19**, 12784–12793 (2017).
- <sup>44</sup>D. Gall, C.-S. Shin, T. Spila, M. Odén, M. J. H. Senna, J. E. Greene, and I. Petrov, J. Appl. Phys. **91**, 3589–3597 (2002).
- <sup>45</sup>A. le Febvrier, D. Gambino, F. Giovannelli, B. Bakhit, S. Hurand, G. Abadias, B. Alling, and P. Eklund, Phys. Rev. B **105**, 104108 (2022).
- <sup>46</sup>G. Ramanath, J. E. Greene, J. R. A. Carlsson, L. H. Allen, V. C. Hornback, and D. J. Allman, J. Appl. Phys. 85, 1961–1969 (1999).
- A. Alman, J. Appl. Phys. 63, 1501–1505 (1999).
   A. Chatterjee, V. Bhatia, A. I. K. Pillai, M. Garbrecht, and B. Saha,
- Mater. Res. Bull. 143, 111443 (2021).

  48B. Biswas, S. Chakraborty, O. Chowdhury, D. Rao, A. I. K. Pillai, V. Bhatia,
- M. Garbrecht, J. P. Feser, and B. Saha, Phys. Rev. Mater. 5, 114605 (2021).

  49M. A. Gharavi, S. Kerdsongpanya, S. Schmidt, F. Eriksson, N. V. Nong, J. Lu,
- M. A. Gharavi, S. Kerdsongpanya, S. Schmidt, F. Eriksson, N. V. Nong, J. Lu, B. Balke, D. Fournier, L. Belliard, A. le Febvrier, C. Pallier, and P. Eklund, J. Phys. D: Appl. Phys. 51, 355302 (2018).
- <sup>50</sup>P. A. Stampe, M. Bullock, W. P. Tucker, and R. J. Kennedy, J. Phys. D: Appl. Phys. 32, 1778–1787 (1999).
- <sup>51</sup>M. A. Gharavi, D. Gambino, A. le Febvrier, F. Eriksson, R. Armiento, B. Alling, and P. Eklund, Mater. Today Commun. 28, 102493 (2021).